Dynamical structure factors of dynamical quantum simulators

Maria Laura Baez[a,b,1], Marcel Goihl[b], Jonas Haferkamp[b], Juani Bermejo-Vega[b,c], Marek Gluza[b], and Jens Eisert[b,d]

[a]Condensed Matter Division, Max Planck Institute for the Physics of Complex Systems, 01187 Dresden, Germany; [b]Dahlem Center for Complex Quantum Systems, Freie Universität, 14195 Berlin, Germany; [c]Departamento de Fisica, University of Granada, 18010 Granada, Spain; and [d]Helmholtz-Zentrum Berlin für Materialien und Energie, 14109 Berlin, Germany

Edited by Peter W. Shor, Massachusetts Institute of Technology, Cambridge, MA, and approved August 26, 2020 (received for review April 2, 2020)

The dynamical structure factor is one of the experimental quantities crucial in scrutinizing the validity of the microscopic description of strongly correlated systems. However, despite its long-standing importance, it is exceedingly difficult in generic cases to numerically calculate it, ensuring that the necessary approximations involved yield a correct result. Acknowledging this practical difficulty, we discuss in what way results on the hardness of classically tracking time evolution under local Hamiltonians are precisely inherited by dynamical structure factors and, hence, offer in the same way the potential computational capabilities that dynamical quantum simulators do: We argue that practically accessible variants of the dynamical structure factors are bounded-error quantum polynomial time (BQP)-hard for general local Hamiltonians. Complementing these conceptual insights, we improve upon a novel, readily available measurement setup allowing for the determination of the dynamical structure factor in different architectures, including arrays of ultra-cold atoms, trapped ions, Rydberg atoms, and superconducting qubits. Our results suggest that quantum simulations employing near-term noisy intermediate-scale quantum devices should allow for the observation of features of dynamical structure factors of correlated quantum matter in the presence of experimental imperfections, for larger system sizes than what is achievable by classical simulation.

quantum simulation | dynamical structure factor | Rydberg atoms | trapped ions

The field of condensed-matter physics has seen a lot of successes aided by powerful computational tools. Classical algorithms, such as Monte Carlo techniques (1), exact diagonalization (2), tensor networks (3), and more, have offered some of the greatest insights into the most surprising behavior of many different systems. The notion of phases and phase transitions is ubiquitous in nature, from condensed matter to cosmology. When a given parameter (such as temperature or magnetic field) is modified, a system can transition from a phase with certain features to another. The overall feature of many of these transitions (though certainly not all) which connects this phenomenon across vast fields of physics is the notion of spontaneous symmetry breaking. For example, for the Ising model we study in this work, the system transitions from a phase exhibiting an underlying $\mathbb{Z}_2$ symmetry to a phase without it—that is, spontaneously breaking $\mathbb{Z}_2$. On the other hand, in the context of particle physics and cosmology, symmetries exist at extremely high temperatures which spontaneously break, leading to the differentiation of fundamental forces (4, 5). The studies of phases and phase transitions is still an open problem in many cases, as the usual analytical techniques are either not enough or not applicable in many cases. At the same time, one would also like to understand their response when time is evolved, which is a complex task from the analytical point. For this reason, many scientists have turned to computer simulations, which carry their own problems in many instances. In this work, we will focus on dynamical aspects of phases and phase transitions to show the power of quantum simulators. By studying the properties of the long-range transverse-field Ising model, a relatively simple system about which we do not understand everything yet, we can show how quantum simulators can access a critical experimental signature which allows one to compare the results of a quantum simulation directly to experiments, be it across a phase transition or away from it.

While current numerical techniques are still extremely useful, in many cases, the system sizes need to be constrained to a couple dozen atomic sites to obtain an efficient simulation, or the algorithms are just efficient for a narrow class of models. This arises from the fact that each one of these physical problems can be connected to a computational problem which belongs to a (in many cases) well-determined complexity class (6). Despite the field slowly pushing the boundaries of what is possible, the complexity boundary cannot be surpassed with classical algorithms. As long as the resource is a classical simulation, and considering certain assumptions believed to be true in the field of complexity theory (7, 8), we know how far we can go. For example, in higher-dimensional frustrated quantum magnets or high-T_c superconductors, we have no generic efficient way of calculating some of the most important quantum expectation values needed to understand the properties of a particular phase of interest. For example, quantum Monte Carlo is a powerful method, but it is affected by strong sign problems for frustrated and fermionic systems (9–11). Exact diagonalization can yield a plethora of useful results for many different physical systems, but the computational resources required scale exponentially in the system size. Other more sophisticated methods, such as matrix

Significance

Quantum simulators promise to offer new insights into strongly correlated matter beyond what is accessible by means of classical computers. We propose dynamical quantum simulators (DQSs) as a method to simulate dynamical structure factors (DSFs) for system sizes considerably larger than what classical simulations can compute and provide complexity-theoretic evidence that they cannot be classically efficiently computed. Based on state-of-the-art experimental setups, we show how results from DQSs can be directly compared to experiments exploring properties of quantum materials. At the same time, we explore long-ranged spin systems: In particular, we show that the DSFs in DQSs can exhibit the signatures of excitation confinement in long-ranged models for which a comprehensive understanding is lacking.

Author contributions: M.L.B., J.B.-V., M. Gluza, and J.E. designed research; M.L.B., M. Goihl, J.H., J.B.-V., M. Gluza, and J.E. performed research; M.L.B., M. Goihl, J.H., and M. Gluza analyzed data; and M.L.B., J.H., J.B.-V., M. Gluza, and J.E. wrote the paper.

The authors declare no competing interest.

This article is a PNAS Direct Submission.

[1]To whom correspondence may be addressed. Email: baez@pks.mpg.de.

This article contains supporting information online at https://www.pnas.org/lookup/suppl/doi:10.1073/pnas.2006103117/-/DCSupplemental.

First published October 2, 2020.

product states (MPS), projected entangled Pair states (PEPS), multi-scale entanglement renormalization ansatz (MERA), etc., are efficient for one-dimensional short-range systems, but these methods are constrained by the amount of entanglement present in the system.

In this work, we propose dynamical analog quantum simulators (12, 13) as an alternative method to simulate low-energy excitations of strongly correlated matter. In particular, we suggest that *dynamical structure factors* (DSFs), which provide key physical insights into quantum matter, can be accessed with quantum simulators, while at the same time are a quantity which is significantly less accessible with classical computers.

Large-scale analog quantum-simulation platforms are unique systems in that they show exceptionally strong quantum effects and allow for measuring expectation values of microscopic observables (14–21). Among other platforms, the propagation of excitations in XXZ models (14, 15), Lieb–Robinson bounds (16), relaxation dynamics (22), and phase diagrams of Fermi–Hubbard models (17) have been probed with ultracold atoms beyond capabilities of current classical algorithms. At the same time, quantum simulations with trapped ions and Rydberg arrays have also seen several breakthroughs, as, for example, the quantum dynamics of the long-range transverse-field Ising model, which has recently been studied in systems of over 50 atoms via time-dependent expectation values of single spin observables (18–21). Though a great body of observations has been assembled, a particular question arises: Can quantum simulators provide qualitative dynamical quantities of systems relevant in the condensed-matter context, for which there is evidence that in the regime discussed they are inaccessible to classical algorithms?

We propose an answer to this question in form of the DSF, a widely attainable experimental observable which gives information regarding dynamical properties of a given system. In materials, it is experimentally measured by inelastic neutron scattering (23) and resonant inelastic X-ray scattering (24). Given the relative ease of measuring the DSF experimentally, an efficient way to simulate this quantity becomes imperative. We argue that the DSF can be accurately accessed with quantum simulators within the experimental level of accuracy currently available in the different architectures and for system sizes beyond what current classical algorithms can achieve, as we show in Fig. 1. It is worth pointing out that in the quantum-simulator setting, there have been previous measures of DSFs (25). The major difference between those studies and ours is that while those proposals rely on a modification of the simulator architecture to measure the DSF (what would be considered a hardware solution), we propose a software solution in which the setup does not need any specific modification to be able to detect DSFs.

The DSF is a quantity which can be considered stable to small perturbations of the microscopic model whose excitations it probes, given that the qualitative features of the DSF already provide a lot of information regarding those excitations. In this sense, we expect to see an inherent robustness in the DSF, finding that observing the signatures of low-energy excitations is possible with state-of-the-art setups in the presence of moderate experimental imperfections. As a proof of principle, we investigate the short-and long-range transverse field Ising model (TFIM). The short-range model is integrable (30) and allows us to study relatively big system sizes comparable to those achievable in trapped ions and Rydberg atoms simulators. We first study in detail the effects of experimental imperfections in the short-range model and the associated Fourier transform involved in the calculation of the DSF to give us an intuition of those effects. Once the short-range model is well understood, we move to our application proposal. The classical numerical calculation of unequal time-correlation functions in long-range systems is constrained to system sizes much smaller than what current quantum simulators can achieve (18, 19). Thus, we propose the measurement of the DSF for the long-range TFIM as a practical application of quantum simulators in a quantity relevant for both condensed matter and material science.

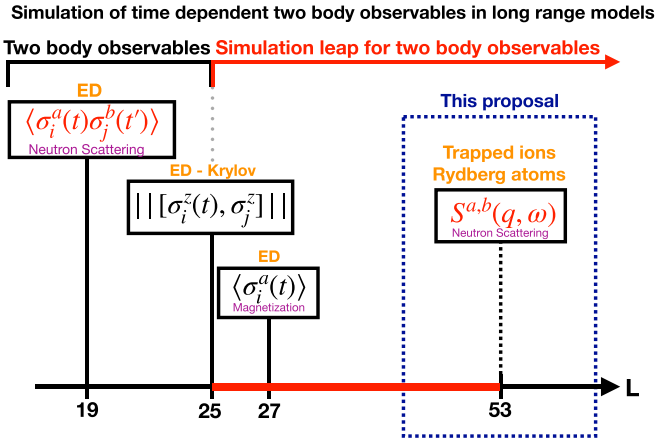

Fig. 1. State-of-the-art exact numerical algorithms to time evolve two-body observables for the long-range TFIM. The larger system sizes for which unequal time correlators (and by extension DSFs) can be accessed are shown. At 19 sites, the Pauli operators at different sites have been time-evolved via exact diagonalization (ED) (26). Using Krylov-space methods, the system size has been extended to 25 (27). System sizes up to 27 (ED) and 128 [Lanczos and time dependent density matrix renormalization group (t-DMRG)] sites have been obtained, but only single-site observables have been accessed (28). Here, we show that our proposal offers a leap forward in terms of the system sizes that can be employed to study DSFs of long-range models via quantum simulation. Please note that using variational methods, entanglement entropies up to 125 sites can be obtained (29).

We study the long-range TFIM under the same imperfections as for the short-range model. We show that the experimental imperfections currently present in quantum simulators do not affect the DSF in a significant way and that the scaling of these errors in the DSF is well controlled in the full range of system sizes studied here.

We also study the computational hardness of evaluating the DSF for general systems. We find that the DSF can be likened to a bounded-error quantum polynomial time (BQP)-hard problem, meaning that any classical algorithm calculating it for general Hamiltonians efficiently would also efficiently solve all of the tasks that a quantum computer can tackle efficiently. The latter is regarded in the quantum-computing community as a highly unlikely scenario. As such, realizing our proposal in practice would tackle a task hard for classical computers in a field of practical importance in condensed-matter physics. While the specific proposal of this work is centered on a specific model, it is worth pointing out that the proof of hardness is valid for a wide range of Hamiltonians. It is our aim in this work to highlight a specific case in which the DSF can be experimentally achieved in the near-term, but the protocol employed here, together with the error analysis and the study of the different architectures, can be easily applied to other models, as, for example, the XY model in superconducting chips (31) or Rydberg atoms (32). As such, future advances in the field, where analog quantum simulators implement further models in higher dimensions, can make use of the study performed in this work to show a practical application of quantum simulators through the DSF in those models.

DSF in Quantum Simulators

In order to employ quantum simulators to study the DSF of solid-state systems, we want to probe the fluctuations of their ground states or thermal states via unequal time correlation functions. For a spin system with lattice sites $i, j \in \Lambda$ (where Λ is the collection of lattice sites), these are defined by

$$C^{a,b}_{i,j}(t) = \langle \sigma^a_i(0)\sigma^b_j(t)\rangle, \quad [1]$$

And we denote Pauli matrices by σ^a with $a = x, y, z$. The Fourier transform of these quantities from real-space sites $\mathbf{x}_i$ to momentum $\mathbf{q} \in \mathbb{R}^3$ and time-to frequency-domain $\omega \in \mathbb{R}$ yields the DSF

$$S^{a,b}(\mathbf{q},\omega) = \frac{1}{N}\sum_{i,j\in\Lambda}\int_{-\infty}^{\infty} \mathrm{d}t\; e^{-\mathrm{i}\mathbf{q}\cdot(\mathbf{x}_i-\mathbf{x}_j)} e^{\mathrm{i}\omega t} C^{a,b}_{i,j}(t), \quad [2]$$

where N is the number of lattice sites. There has been a recent proposal (33) on how to measure retarded Green's functions (which are related to the DSF in equilibrium via the fluctuation-dissipation theorem) in cold atoms and trapped-ion devices using *Ramsey spectroscopy*; however, a clear understanding of the feasibility of observing important physical effects and the DSF itself, when the proposal of ref. 33 is applied to a quantum many-body system is still lacking.

In Fig. 2, we show a typical DSF for the TFIM, one of the models we will study in detail in this work, away from criticality. In the figure, we observe a cosine-shaped continuum, with a gap at $q = 0$. The goal of this work is to show that a DSF like the one in Fig. 2 can be obtained from state-of-the-art quantum simulations.

To obtain such a DSF in quantum simulators, the crucial ingredient that needs to be supplemented beyond the existing techniques is a measurement protocol which gives access to unequal time-correlation functions, as in Eq. **1**. In the following, we propose a generalization of the protocol proposed by ref. 33, which can be employed in any setup where a single-site spin rotation can be implemented. We extend this spectroscopy protocol via tomographic methods to systems which do not exhibit as many symmetries as ref. 33 assumes. In this context, we offer a measurement protocol which can be implemented in many different architectures, as trapped ions, Rydberg atoms, and superconducting qubit chips, and for a wide class of systems beyond Ising and XXZ, as has been proposed (33).

DSF Measurement Protocol. The DSF effectively probes low-energy excitations of a given system, described by a particular Hamiltonian H. Given the definition of the DSF in Eq. **2**, the excitations to which it is sensitive are those related to observables of the form given in Eq. **1**. The first step to obtain such a quantity then resides in the initialization of the quantum simulator in a low-energy state, ideally the ground state of H. In this section, we will assume, for the sake of simplicity, that the quantum simulator will be initialized in the unique ground-state vector of H, which we refer to as $|\psi_0\rangle$, though in principle, the protocol we employ can be used with any initial state, be it in equilibrium or not, as exemplified in ref. 34 with the Ramsey spectroscopy technique.

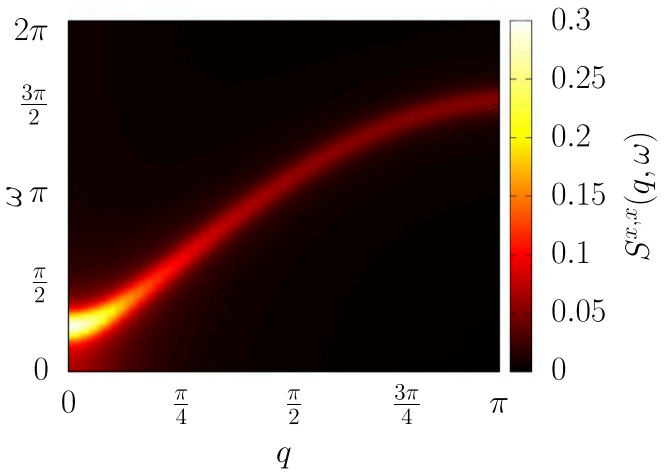

Fig. 2. DSF for the TFIM. We show the DSF away from the criticality, $J = 1$ and $B = 1.4$. We observe the gap around the $q = 0$, $\omega = \pi/4$ point, and the ω-dependent two-particle continuum extending over the entire reciprocal space, in accordance with the exact solution of the TFIM (30).

Preparing such a state can be achieved by adiabatic evolution. At the same time, the recently proposed *quantum approximate optimization algorithms* (QAOAs) can also been employed. These algorithms have recently been reported in trapped-ions experiments (35), achieving a very good approximation of the ground state of nontrivial Hamiltonians. It is worth pointing out that QAOAs have been shown to considerably reduce the experimental time required for ground-state preparation in comparison to adiabatic evolutions in trapped ions, effectively extending the evolution times which can be achieved with this particular architecture.

Once the ground state is obtained, we then induce low-energy excitations by applying a single spin rotation. After exciting the system locally, the state is *evolved* with the Hamiltonian H. Finally, after the evolution, we measure local spin operators with single-site resolution. Once the unequal time correlators are measured, the DSF can be obtained via a spatial and temporal Fourier transform.

Measuring Unequal Time Correlations. Let us now discuss the crucial question at hand: How can we measure two-point unequal time correlation functions if we can only perform unitary transformations and measure local spin operators? The main insight of ref. 33 [see also ref. 34 for a detailed study of the idea] has been that the operator at initial time $\sigma^a_i(0)$ can be obtained as part of a unitary operation, the pulse of *Ramsey interferometry*.

We begin by the basic, and at the same time most important, example of this idea: Consider the unitary representing a $\frac{\pi}{4}$-rotation of a spin at site $j \in \Lambda$ along the x axis

$$U^{(j)} = \frac{1}{\sqrt{2}}(\mathbb{1} - \mathrm{i}\sigma^x_j). \quad [3]$$

We would like to use it as an excitation of a low-energy-state vector $|\psi_0\rangle$, which then is probed by subsequent evolution $U(t)$ to time t governed by the many-body Hamiltonian of the interacting system being investigated. To keep the discussion simple, let us assume that the expectation value of an odd number of spin operators vanishes for $|\psi_0\rangle$ [as is the case for the TFIM and arises from the symmetries of the Hamiltonian and initial state (33)].

Having these two ingredients at hand, we can consider the state vector

$$|\psi\rangle = U(t)\,U^{(j)}\,|\psi_0\rangle\,, \quad [4]$$

which can be obtained by an appropriate unitary single-qubit rotation $U^{(j)}$ that locally excites the system (as the one in Eq. **3**) and a subsequent time evolution of the system $U(t)$. Observe that both operations are unitary, and, thus, $|\psi\rangle$ is a state vector. If we measure the expectation value of σ^x_i on this state, we obtain

$$\langle\psi|\,\sigma^x_i\,|\psi\rangle = \frac{1}{2}\,\langle\psi_0|\,\sigma^x_i(t)\,|\psi_0\rangle + G^{\mathrm{ret}}_{x,x}(i,j,t) + R(i,j,t), \quad [5]$$

with $R(i,j,t) = \frac{1}{2}\,\langle\psi_0|\,\sigma^x_j\sigma^x_i(t)\sigma^x_j\,|\psi_0\rangle$, and $G^{\mathrm{ret}}_{x,x}(i,j,t)$ the retarded Green function

$$G^{\mathrm{ret}}_{x,x}(i,j,t) = -\frac{\mathrm{i}}{2}\langle\sigma^x_i(t)\sigma^x_j(0) - \sigma^x_j(0)\sigma^x_i(t)\rangle_0. \quad [6]$$

The first term in the last line of Eq. **5** can be measured directly by simply omitting the excitation step and, hence, can be subtracted from the data if it is nonzero. The last term, on the other

hand, has a nontrivial unequal time dependence and, hence, must either vanish due to, e.g., symmetry arguments or has to be reconstructed.

The case considered in ref. 33 is the one in which the Hamiltonian $\hat{H}$ has a unitary symmetry $\mathcal{P}$, such that the product of an odd number of Pauli operators vanish. From this, it follows that $R(i,j,t)$ must vanish. As such, whenever a symmetry of this kind is present (as in the TFIM), we obtain the identity $\langle\psi|\,\sigma_i^x\,|\psi\rangle = G^{\mathrm{ret}}_{x,x}(i,j,t)$. Calculating this for all spin pairs (i,j), we obtain the retarded Green function $G^{\mathrm{ret}}_{x,x}(i,j,t)$, and we can perform a Fourier transform in real space and time to obtain $G^{\mathrm{ret}}_{x,x}(\mathbf{q},\omega)$. Finally, we can relate the retarded Green function, when linear response theory holds, to the DSF via the fluctuation-dissipation theorem

$$S^{xx}(\mathbf{q},\omega) = -\frac{1}{\pi}[1+n_B(\omega)]\mathrm{Im}[G^{\mathrm{ret}}_{x,x}(\mathbf{q},\omega)], \qquad [7]$$

where $n_B(\omega) = 1/(e^{\omega/T}+1)$. This way, we get direct access to the DSF by measuring the retarded Green's function via the above measurement protocol.

There are two points which need to be made before we move on: First, while we study the zero-temperature DSF, finite, but small, temperatures will broaden the features of the DSF, but not change the overall behavior, provided that T is smaller than the smallest coupling of the model. Second, note that the fluctuation-dissipation theorem holds when linear response theory is a good approximation, and its validity or lack of thereof away from equilibrium is a highly researched topic to the date (13, 36, 37). As such, this measurement protocol for the DSF will be accurate when the system is close to thermal equilibrium in a practical sense.

Tomographic Recovery Methods for Unequal Time-Correlation Functions. If the symmetry argument can be relaxed, we can show how the term $R(i,j,t)$ can be extracted. Let us define a modified Ramsey state vector which reads

$$|\psi_\phi\rangle = U(t)\,U^{(j)}(\phi)\,|\psi_0\rangle\,, \qquad [8]$$

where now we excite the ground state $|\psi_0\rangle$ with a ϕ-rotation around the x axis

$$\begin{aligned} U^{(j)}(\phi) = e^{-\mathrm{i}\phi\sigma_j^x} &= \cos(\phi)\mathbb{1} - \mathrm{i}\sin(\phi)\sigma_j^x \\ &=: c_\phi\mathbb{1} - \mathrm{i}s_\phi\sigma_j^x. \end{aligned} \qquad [9]$$

For an analogous measurement to the case in the previous section, we obtain

$$\begin{aligned} \langle\psi_\phi|\,\sigma_i^x\,|\psi_\phi\rangle = c_\phi^2\,\langle\psi_0|\,\sigma_i^x(t)\,|\psi_0\rangle + 2c_\phi s_\phi G^{\mathrm{ret}}_{x,x}(t) \\ + s_\phi^2 R(i,j,t). \end{aligned} \qquad [10]$$

We now notice that we can directly measure the left-hand side and the first term on the last line of the expression above. For a fixed angle ϕ, we can write

$$b_\phi = \langle\psi_\phi|\,\sigma_i^x\,|\psi_\phi\rangle - c_\phi^2\,\langle\psi_0|\,\sigma_i^x(t)\,|\psi_0\rangle\,. \qquad [11]$$

Now, we can rewrite Eq. **10** as

$$a_\phi^T v = b_\phi, \qquad [12]$$

where v is the vector we want to reconstruct, given by

$$v = [G^{\mathrm{ret}}_{x,x}(t), R(i,j,t)]^T, \qquad [13]$$

and $a_\phi = [2s_\phi c_\phi, s_\phi^2]$. If an experiment measures b_ϕ using various angles ϕ, then we can build a matrix A using the different a_ϕ's as rows, and, in a corresponding fashion, we can collect the measured b_ϕ's into a vector b.

The retarded Green's function can be reconstructed by noticing that

$$v^\star = (A^TA)^{-1}A^Tb, \qquad [14]$$

gives the value of v that minimizes the least-square residue

$$\min_v \|Av-b\|_2. \qquad [15]$$

Here, we assume that one can choose the excitation angles ϕ in such a way that the matrix A^TA is well conditioned, as is done in typical tomographic schemes. In order to measure the DSF, this procedure must be performed for all pairs of excitation and measurement positions $i,j\in\Lambda$, and the Fourier transform of the collection of reconstructed values $v_1^\star = G^{\mathrm{ret}}_{x,x}(i,j,t)$ will yield the DSF.

On the Computational Complexity of the DSF

Once we have formalized how dynamical quantum simulators can access the DSF, we will concentrate on answering the question: In what specific way is the calculation of the DSF a computationally hard problem? In the following, we formalize the statements about classical hardness and show that a practically accessible variant of the DSF is hard for the complexity class BQP. To this end, we show that the building blocks of the DSF, the unequal time correlators $C_{i,j}^{a,b}(t)$, are BQP-hard to compute.

To start with, and without loss of generality, we show that $\langle\sigma_i^z(t)\sigma_j^z\rangle_\psi := \langle\psi|\,\sigma_i^z(t)\sigma_j^z\,|\psi\rangle$ is BQP-hard to compute for product-state vectors $|\psi\rangle$ and for ground states. Then, we use these observations to consider the DSF over a finite (but arbitrarily large) interval of time

$$S^{z,z}_{t_0,t_1}(q,\omega) = \frac{1}{N}\sum_{i,j}\int_{t_0}^{t_1} e^{-\mathrm{i}q(x_i-x_j)}e^{\mathrm{i}\omega t}\,\langle\sigma_i^z(t)\sigma_j^z\rangle_\psi\,\mathrm{d}t, \qquad [16]$$

where N is the system size. In particular, we prove the following.

Theorem 1 (Hardness of Computing the Approximate DSF). *For $t_1 - t_0 = \mathrm{poly}(N)$, product states $|\psi\rangle$, and two-local Hamiltonians it is BQP-hard to approximate $S^{z,z}_{t_0,t_1}(q,\omega)$ within an error $\varepsilon = \mathrm{poly}'^{-1}(N)$.*

We consider the quantity $S^{z,z}_{t_0,t_1}$ instead of the full Fourier transform, as it is the practically accessible one: Any time observation will necessarily be finite in practice. What is more, from a conceptual perspective, the latter is not even computable on a Turing machine due to arbitrarily large errors that are introduced by the Fourier transform: The continuous Fourier transform is not Turing computable.

Hardness for estimating correlators on ground states. For hardness of ground states, we observe that computing $C_{i,j}^{z,z}(t) = \langle\sigma_i^z(t)\sigma_j^z\rangle_\psi$ for any t is at least as hard as computing $C_{i,j}^{z,z}(0) = \langle\sigma_i^z\sigma_j^z\rangle_\psi$. First, computing correlators up to constant additive errors on ground states of quasi-local Hamiltonians is BQP-hard by the Feynman–Kitaev construction (38). Furthermore this remains true for several classes of local observables and local Hamiltonians, including one-local observables measured on ground states of nearest-neighbor two-local Hamiltonians on qubits (39, 40) and two-local observables measured on ground states of translation invariant nearest-neighbor two-local Hamiltonians with local dimension three (41).

Hardness for out-of-time correlators. For the product states, we start with a general observation: Consider an arbitrary circuit $C_n = U_n\ldots U_1$ consisting of k-local gates U_i. Evaluating the quantity $\langle\sigma_i^z(t)\sigma_j^z\rangle_\psi$ for product-state vectors $|\psi\rangle$ within

constant error is BQP-hard. Here, $0 \leq t \leq n$ is an integer. For $\Pr(1)$, the probability of measuring one, we obtain

$$\Pr(1) = \langle\psi|\, C_t^\dagger \left(\frac{1+\sigma_i^z}{2}\right) C_t\, |\psi\rangle = \frac{1}{2} \pm \frac{1}{2} \left\langle \sigma_i^z(t)\sigma_j^z \right\rangle_\psi .$$

Here, $|\psi\rangle$ is assumed to be in the σ^z-eigenbasis. The sign in the above calculation can be immediately obtained from $|\psi\rangle$. Computing the above probability within a constant additive error suffices to yield a valid reduction to the output probabilities of quantum circuits. We are interested in the case where the circuit C_t is given by the time evolution $e^{\mathrm{i}tH}$ for some Hamiltonian H.

The definition of the DSF is given for continuous time (Eq. **2**), but quantum simulators (and also classical simulations) need to discretize time, as the measurement protocols proposed cannot continuously measure $C_{i,j}^{z,z}(t)$, but require a fresh preparation for each point in time. In the following, we show that while this discretization leads to errors, they are bounded.

The discretization error. Notice that there will always be an error from the discretization of time. However, this can be bounded: For any differentiable function f, we can use the mean-value theorem to obtain

$$|f(t+\delta t) - f(t)| \leq \left| \max_{t' \in [t, t+\delta t]} \partial f(t') \right| \delta t. \qquad [17]$$

For $C_{i,j}^{z,z}(t) = \left\langle \sigma_i^z(t)\sigma_j^z \right\rangle_\psi$, we have

$$\begin{aligned} |\partial_t C_{i,j}(t)| &= \left| \left\langle \psi \left| \partial_t \left(\sigma_i^z(t)\sigma_j^z\right) \right| \psi \right\rangle \right| \\ &= \left| \left\langle \psi \left| \partial_t \left(e^{\mathrm{i}tH} \sigma_i^z e^{-\mathrm{i}tH} \sigma_j^z \right) \right| \psi \right\rangle \right| \\ &= |\mathrm{i} \left\langle \psi \left| e^{\mathrm{i}tH} [H, \sigma_i^z] e^{-\mathrm{i}tH} \sigma_j^z \right| \psi \right\rangle| \leq L' = \mathrm{const}, \end{aligned} \qquad [18]$$

where we use the fact that we assume H to be a (geometrically) local Hamiltonian, and L' is the Lipshitz constant. Thus, $H = \sum_{i=1}^r h_i$ with $r = \mathrm{poly}(N)$ and $\|h_i\|_\infty \in \mathcal{O}(1)$, and, furthermore, σ_i^z commutes with all but constantly many summands h_j. The inequality thus follows from the triangle inequality and the submultiplicativity of the operator norm. It hence suffices to choose a constantly small discretization step to bound this error. In particular, this proves that $C_{i,j}^{z,z}(t)$ is Lipshitz-continuous with size-independent Lipshitz constant.

Hardness for a variant of the DSF. The *discrete DSF* is defined as

$$\tilde{S}^{z,z}(q,\omega) = \frac{1}{N} \sum_{i,j} \sum_{k=1}^{M} e^{-\mathrm{i}q(x_i - x_j)} e^{\mathrm{i}\omega(t_0 + k\Delta t)} \left\langle \sigma_i^z(t_0 + k\Delta t)\sigma_j^z \right\rangle, \qquad [19]$$

with $\Delta t = (t_1 - t_0)/M$. Notice that this is the quantity that is usually approximated in numerical simulations. Computing the discrete Fourier transform can be done via the *fast Fourier transform*, which runs in time $\mathcal{O}(\ln(M)M)$ for $M = \mathrm{poly}(N)$. Hence, if the correlators are BQP-hard, the discrete DSF is as well.

We can bound the error on the continuous DSF as well if only a finite interval of time is involved. We know that $C_{i,j}^{z,z}(t) = \left\langle \sigma_i^z(t)\sigma_j^z \right\rangle_\psi$ is a function with polynomially bounded Lipshitz constant. For a bounded interval of time $[t_0, t_1]$, we consider the error that occurs by approximating the integral in Eq. **16** with step functions

$$S_{t_0,t_1}^{z,z}(q,\omega) \approx \frac{1}{N} \sum_{i,j} \sum_{k=1}^{M} e^{-\mathrm{i}q(x_i - x_j)} e^{\mathrm{i}\omega t_0 + k\Delta t} C_{i,j}^{z,z}(t_0 + k\Delta t)\Delta t, \qquad [20]$$

where $\Delta t = t_1 - t_0/M$. Integrating over the error made by the step-function approximation gives us the cumulated error $(t_1 - t_0)L'\Delta t = (t_1 - t_0)^2 L'/M$, where L' is the Lipshitz constant of the function $e^{-\mathrm{i}q(x_i - x_j)} e^{\mathrm{i}\omega t} C_{i,j}^{z,z}(t)$. Hence, choosing M to be constant and small suffices for an approximation within arbitrarily small constant error. In essence, we have proven that $C_{i,j}^{a,b}(t)$ and $S^{a,b}(q,\omega)$ are BQP-hard in a specific sense. Furthermore, since simulations both classical and quantum require a discretization of the time axis, we have shown that the possible errors from this are well behaved and controlled.

BQP-hardness provides evidence against the existence of classical algorithms that compute DSFs in polynomial time. However, it is important to point out that this is a so-called worst-case result—i.e., it only rules out an algorithm that solves all cases in polynomial time. In general, subclasses of this problem are not necessarily hard in the complexity theoretic sense. For example, the time evolution of the nearest-neighbor, short-range, transverse Ising model is not expected to be universal for time evolution.

Practical Realization of DSFs in Quantum Simulators

So far, we concentrated on how the previously mentioned measurement protocol can be employed to obtain DSFs and on the complexity of this task. To assess the degree of robustness of DSFs against experimental imperfections, we will study the short- and long-range TFIMs in the presence of those imperfections. The translational invariant 1D-TFIM is defined as

$$H(J,B) = \sum_{i \in \Lambda} B_i \sigma_i^z - \sum_{i,j \in \Lambda} J_{i,j} \sigma_i^x \sigma_j^x . \qquad [21]$$

The coupling parameters of the Ising term are $J_{i,j}$, and, in principle, can be site-dependent. The strength of the magnetic field is given by B_i, and in this work, we will consider it uniform throughout the chain, $B_i = B$. The spin–spin interaction can take the long-range form $J_{i,j} = J/|i-j|^\alpha$ for analog quantum simulations in Rydberg arrays or trapped ions, where typically $\alpha \in [1, 6]$ (*SI Appendix*, section I). In the case of digital simulation and optical lattices, one can study the short-range model (17) with $J_{i,j} = J\delta_{i,j\pm 1}$, which is exactly solvable by a mapping to noninteracting fermions (30).

While our proposal is focused on the long-range model, the access to the DSF via quantum simulation for the short-range case is of great importance for two main reasons. First, the short-range model is much better understood than the long-range counterpart, and, as such, a study of its DSF can provide helpful insights on the effects of the different imperfection models, as well as on the accuracy of the measurement protocol which can be expected. Since the short-range model is an easy instance of the time-evolution problem, we perform a detailed study of the effects of the evolution imperfections in this case. This way, we can provide sufficient understanding of the expected effects of these imperfections on the quantum simulation of the DSF. After this task is completed, we can move on to study the long-range model and evaluate our practical proposal. Second, several architectures as optical lattices or Rydberg arrays can access the short-range model, or the long-range model at high values of α, where the system effectively behaves short-range. Our study of the short-range model thus provides data which can be directly used to compare with experiments on those platforms.

Universal Properties of the Short-Range TFIM. The physics of the short-range, nearest-neighbor TFIM has been studied in detail (30). Here, we will briefly describe the low-energy excitations of the TFIM and their signature in the DSF in terms of a two-kink model.

For the short-range TFIM in the ferromagnetic phase, the ground state is given by a product state of spins fully polarized.

When the magnetic field and Ising coupling are at a finite value, fluctuations are induced in the system, in the form of fermionic pseudo-particles γ. These excitations can be seen in the spin picture as spin flips, or kinks over the fully polarized state. Once a spin is flipped, it is free to move along the chain and create a domain. The walls of this domain can be regarded as the kinks (or, equivalently, the γ-fermions) that interpolate between the two possible ground states connected by the $\mathbb{Z}_2$ symmetry of the model. When a domain is formed, the domain walls or kinks behave as free fermionic particles that propagate through the chain. Since to create a domain, we need at least two kinks (particles), the first contribution to the excitation spectrum will come from the two-particle states, which will be described by their energy and momenta, $E = \epsilon_{q_1} + \epsilon_{q_2}$ and $q = q_1 + q_2$. For a fixed q, the values of q_1 and q_2 can be chosen arbitrarily, which generates a continuum of excitations.

The spectrum of excitations will manifest in the DSF: Studying the longitudinal xx-structure factor, $S^{xx}(q,\omega)$, we observe the gap, and the continuum of excitations (the so-called two-particle continuum) that corresponds to the two-particle states we mentioned previously. This observations have been shown, both numerically (43) and experimentally via neutron scattering (23). In Fig. 2, we show the xx-DSF for the short-range TFIM, as obtained from our free-fermionic calculation for $J = 1$ and $B = 1.4$, for 50 sites. We clearly observe the two-particle continuum which characterizes the low-energy fluctuations, as well as the excitation gap at the point $q = 0$, $\omega \sim \pi/4$ (in units of J).

Long-Range TFIM. We can now concentrate on the case which is our test of a practical application: the long-range TFIM. Models with these kind of long-range interactions present considerable challenges to numerical studies. The long-range interactions severely constrain the system sizes which can be studied with exact diagonalization techniques based on sparse matrices. Furthermore, studies of these systems employing finite-size MPS-based techniques (44, 45) are affected by severe finite-size effects arising from the entanglement cutoffs required by these approaches. Recently, however, there has been success in studying the statics of long-range models employing MPS algorithms, which directly act in the thermodynamic limit, such as iDMRG (44, 46).

At the same time, several algorithms which can time-evolve an MPS with long-range interactions have been proposed (47, 48) to study the long-range TFIM (49). With the advent of these new techniques, and the state-of-the-art quantum simulators capable of implementing long-range TFIMs, the question of whether the DSF of this class of models can be accessed with these experimental architectures naturally arises.

In the case of the long-range TFIMs, while the ground-state phase diagram has been explored (50–52), much less is known about its dynamical behavior (53–55). Recent studies (27, 29, 56) concentrate on the entanglement growth and the spread of correlations in this model as a function of the interaction length, α, or in the thermalization of different initial states under this Hamiltonian (28). Analyzing the light cones and possible Lieb–Robinson-like bounds in the long-range TFIM at zero temperature, these studies separate the dynamical behavior of this model in three regions. For $\alpha > 3$, the system obeys the generalized Lieb–Robinson bound (57), and the behavior of the system mimics that of a short-range model. Via semiclassical arguments, the dispersion relation of excitations in the ground state (what we study here via the DSF) is found to approximately be a cosine, which coincides with the short-range behavior. From this, we can say that for quantum simulators, the behavior of the DSF in the regime $\alpha > 3$ is expected to be very close that of the short-range model. On the other hand, in the range $1 < \alpha < 3$, a broad light cone is observed and an excitation dispersion which is bounded. This case is of special interest in this work, since trapped-ion experiments can implement long-range TFIMs in this range, but also given that it has recently been shown (26, 42, 58) that in this regime the long-range interactions introduce an effective attractive force between a pair of domain walls. This attractive force confines the excitations in bound states analogous to the confinement of mesons in high-energy physics (26, 42, 58). Since this exotic physics can be probed studying the confinement signatures in both the unequal time correlators and DSFs, our work opens the door to the study of these effects in quantum simulators. Finally, we mention that for $\alpha < 1$, the light cone completely disappears and a virtually instantaneous spread of correlations is observed. In Fig. 3, we show the DSF of the long-range TFIM, as obtained numerically from a full exact diagonalization of a system of 14 spins at zero temperature, for the interaction lengths $\alpha = 1$ (Fig. 3*A*), 2 (Fig. 3*B*), and 3 (Fig. 3*C*). In this figure, we see that for $\alpha = 1$, the DSF shows no ω-dependence, which hints at the possibility of excitation confinement (26, 42, 58) being evidenced through the DSF. For $\alpha > 2$, the ω dependence is recovered, slowly approaching the short-range behavior as α is increased.

Imperfection Models. Three basic ingredients are needed to simulate DSFs on near-term devices: First, we need to be able to prepare the ground state of the target Hamiltonian in a controlled way, and ideally with as high-state fidelity as possible. Second, we need to be able to control the time evolution of the system, in such a way that the physics we desire to investigate is not severely mitigated by experimental imperfections. And,

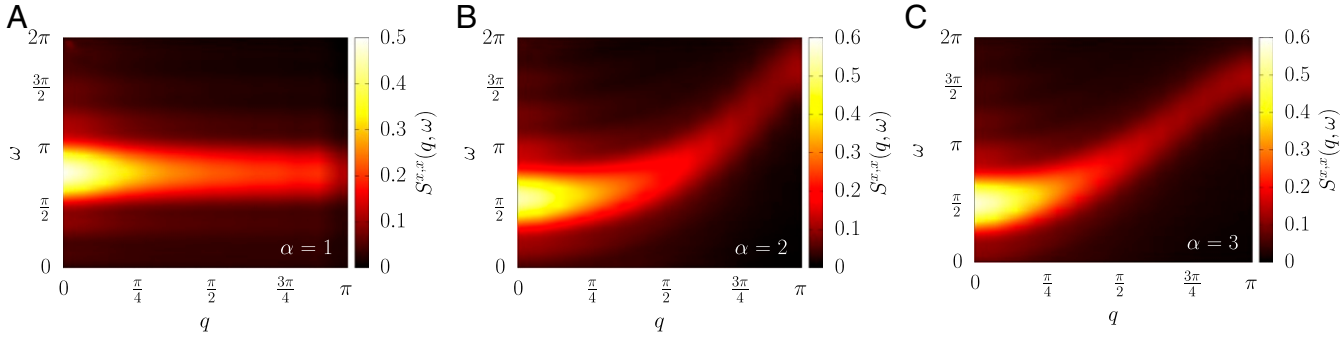

Fig. 3. DSF for the long-range TFIM, for the cases $\alpha = 1$ (*A*), 2 (*B*), and 3 (*C*). For the case $\alpha = 1$, we see that the DSF does not vary in frequency, which is a possible signature of excitation confinement, in accordance with refs. 26 and 42. For $\alpha > 2$, the two-particle continuum is noticeable, and the gap is lowered. As the value of α is increased, the interactions become shorter-range, and the gap approaches the value for the short-range model. Accordingly, the continuum changes shape, from the absence of ω dependence for $\alpha = 1$ toward the cosine form at $\alpha = 3$. This cosine shape corresponds to the short-range TFIM, obtained in the limit $\alpha \to \infty$. For comparison with the short-range TFIM, please refer to Fig. 2.

finally, we want to employ the proposed measurement protocol to determine the unequal time Green functions. Every one of these steps carries their own imperfections, which we will consider separately.

For the preparation imperfections, we will study the effect of measuring DSFs when the prepared state has a fidelity with respect to the ground state smaller than one, $F = \langle \psi_\sigma | \psi_0 \rangle < 1$. The measurement protocol is not modified by this imperfection model, such that even if the prepared state is not the ground state, we can still recover the retarded Green's function via Eq. **7**.

In the case of evolution imperfections, we will study three fundamental effects over the TFIM Hamiltonian. In the first case, we will study how a time-dependent modulation of the Ising couplings affects the DSF. In this case, the Hamiltonian couplings are modified to be time-dependent and of the form

$$J_{i,j} = \frac{J(0)}{|i-j|^\alpha}(1 + A\sin(wt)), \quad J_{i,i\pm1} = J(0)(1 + A\sin(wt)), \tag{22}$$

with $J(0) = J$, for the long- and short-range models, respectively. We will study several modulation amplitudes, $A = 0.01$, 0.05, 0.1, and 0.5, and different frequencies ω between 0.05 and 25.

We will also study the case of random interactions and magnetic fields, related to lattice imperfections. In these cases, the Hamiltonian takes the form in Eq. **21**, but for the case of random interactions, the Ising couplings take the form

$$J_{i,i\pm1} = (J + A\xi_{i,j}), \quad J_{i,j} = \frac{J + A\xi_{i,j}}{(i-j)^\alpha}, \tag{23}$$

for the short- and long-range models, respectively. While in the case of random transverse fields,

$$B_i = B + A\xi_i. \tag{24}$$

In all cases, ξ is drawn independently at random at each site, from a uniform distribution on the interval $[0.0, 1.0)$ with $A = 0.01$, 0.04, 0.1, and 0.4. We employ between 50 and 100 disorder realizations per data point.

Effect of Experimental Imperfections on the DSF of the Short-Range TFIM

In the following, we will demonstrate that the qualitative and quantitative features of the DSF for both the short- and long-range TFIM can be recovered from a quantum simulation even in the presence of experimental imperfections. Here, we discuss the role of imperfections and their impact as such; the certification of the actual correctness of the quantum simulation (59) is a separate task.

To phenomenologically and briefly summarize the results: We show that, at the experimental levels of control present in state-of-the-art architectures, the errors which would be produced in a measurement of the DSF for both short- and long-range TFIM are small, and one can trust both the qualitative and quantitative results of such experiments. Since the overall behavior of the DSF is what gives one information about low-energy excitations of a given system, and how they behave, the errors studied show that, at the current level of experimental control (when our imperfection parameter is set below 5%), the DSF is well behaved. Thus, the overall form of the DSF does not change, and one can safely extrapolate, from a quantum simulation via the DSF, what some of the low-energy excitations of a given model are and what their behavior is.

Quantifying Imperfections. To assess what the effect of experimental imperfections is on the DSF, we will analyze two particular quantities based on the absolute error of the DSF. We define the absolute error as

$$\Delta S(q,\omega) = |S^{x,x}(q,\omega) - \tilde{S}^{x,x}(q,\omega)|, \tag{25}$$

where $S^{x,x}(q,\omega)$ is the DSF obtained from the exact solution of the TFIM in the absence of imperfections. $\tilde{S}^{x,x}(q,\omega)$ is the DSF obtained from the exact solution with various perturbations in the Hamiltonian, arising from the different imperfection models. If we integrate over frequency (reciprocal space), we obtain the average error in reciprocal space (frequency),

$$\Delta S(q) = \frac{1}{N_\omega}\sum_\omega \Delta S(q,\omega), \quad \Delta S(\omega) = \frac{1}{L^2}\sum_q \Delta S(q,\omega), \tag{26}$$

where N_ω is the number of frequencies, which depends on the discretization of the time evolution, and L is the system size. We show the average error for different imperfection models in *SI Appendix*. The maximum of the absolute error, for fixed ω or q, will be denoted by

$$\max_q[\Delta S(q,\omega)], \quad \max_\omega[\Delta S(q,\omega)]. \tag{27}$$

These errors can be understood in the following way: Eq. **25** is the absolute error of the DSF when imperfections are considered. If one makes a cut on the absolute error at a given value of reciprocal space, q, and integrates it over frequency, one obtains the frequency integrated error, $\Delta S(q)$. This is equivalent for cuts at a given frequency ω, to obtain $\Delta S(\omega)$. If, on the other hand, one selects the maximal error at that value, one obtains Eq. **27**. The study of the imperfections in this way allows us to account for the effects in frequency and reciprocal space separately. If the imperfection models do not change the DSF, then these errors should be small and flat over the entire q and ω range. On the other hand, if these errors are not small, we can assess what their effect is on the DSF by studying the shape of the quantities given in Eqs. **26** and **27**. For example, if one of these imperfection models were to close the gap, we would see errors toward small frequencies, but not on q-space.

Since the Fourier transform is performed as data processing over the correlators, we will compare the error of the DSF to the error in the correlators, as to assess the robustness of the Fourier transform. The error in the correlators and the average and maximum over space (where space is indicated as $r = i - j$) are defined as

$$\Delta C_r(t) = |C_r^{x,x}(t) - \tilde{C}_r^{x,x}(t)|, \tag{28}$$

$$\Delta C(t) = \frac{1}{L^2}\sum_r \Delta C_r(t), \quad \max_r[\Delta C_r(t)]. \tag{29}$$

Finally, to determine the scaling properties of the long-range model, we will study the integrated DSF error ΔS as a function of size and of the range of the interactions α, where the integrated error is given by

$$\Delta S = \frac{1}{N_\omega}\frac{1}{L^2}\sum_\omega\sum_q \Delta S(q,\omega). \tag{30}$$

Influence of State-Preparation Imperfections on the DSF. We will concentrate on two architectures, trapped ions and Rydberg atom arrays. Both of them can prepare the initial state via an adiabatic evolution. Furthermore, trapped ions can prepare it through quantum approximate optimization techniques (35). We will study here how the DSF is affected by different evolution times, when the final field value is far away from the quantum critical point, $J = 1$ and $B = 1.4$.

Adiabatic time evolution. The question that motivates us is how the features of the DSF change when the system is prepared for a time τ_Q (the preparation time) from an initial polarized state (which corresponds to the $B \to \infty$ limit) to the final state $B = 1.4$. In the thermodynamic limit, this preparation time diverges when one approaches the quantum critical point. For a finite system, it can be shown that the finite size gap destroys the divergence, and a finite bound on the preparation time can be obtained (60, 61) within which the evolution remains adiabatic.

Considering our previous discussion, it is imperative that we study how the properties of the DSF change when the preparation is not adiabatic. In this case, if the preparation time is not large enough to be in the adiabatic regime, the quantum simulation can still be able to obtain results which are close to the physics that one desires to study. This can be understood, and generalized to preparation protocols beyond adiabatic evolutions, in the context of prepared state fidelity. If the fidelity is high, then the properties of the DSF evaluated over the prepared state will remain close to the properties of the DSF evaluated over the exact ground state. Furthermore, if the preparation evolution is not adiabatic, but does not surpass the quantum critical point, then there exists a time interval in which the transition probabilities toward excited states is sufficiently small, such that the main contribution to the state of the system is the ground state (60–64). At the parameter values studied here, the fidelity of the prepared state F can be thought of as the probability that no extra domain walls (or, equivalently, kinks) have been created during the preparation. Ref. 61 calculates the fidelity of the final state with respect to the vacuum of excitations for a linear ramp, effectively probing the probability that no excitations have been created during the preparation. We find that the fidelity takes the form

$$\ln(1 - F) = -\pi\Delta^2/(4B/\tau_Q). \qquad [31]$$

With this in mind, we can simply ask the question of: How large does τ_Q need to be such that $F \sim 1$, and what are the effects on the DSF when $F < 1$?

We quantify the robustness of the DSF to preparation imperfections employing the error measures shown before. For this, we numerically calculate the DSF of the short-range TFIM, when we prepare the state by a total time τ_Q, starting with the field at $B_{\text{ini}} \to \infty$ and finishing at $B_{\text{final}} = 1.4$.

The adiabatic evolution has been performed for different evolution times, ranging from $\tau_Q = 0.005$ to $\tau_Q = 3000$. In Fig. 4, we show the error analysis for preparation times $\tau_Q = 0.5$, 1, 10, and 100. Following the calculations of ref. 61, we estimate that the fidelity of the prepared state (assuming no other error sources) will correspond to $F \sim 0.043$ for a preparation time of $\tau_Q = 0.5$, to $F \sim 0.59$ for $\tau_Q = 10$, and $F \sim 0.99$ for $\tau_Q = 100$. Our numerical error analysis of the DSF and correlators coincides with these fidelity estimates. We tackle the DSF first: In Fig. 4, *Left*, we show a typical DSF for a preparation time $\tau_Q = 0.5$, and in Fig. 4, *Right*, we show the maximum error of the DSF over frequency (main image) and reciprocal space (*Inset*). For $\tau_Q = 100$, the maximum error is below 5% and mostly flat over the entire (ω, q) space, indicating that this τ_Q is enough to obtain an accurate DSF. This can be confirmed by comparing Fig. 4, *Left* and Fig. 2. From these figures, we notice that the discrepancy in the DSF between the exact case and the one studied in this section appears around the point $(q = 0, \omega = \pi/4)$, which corresponds to the position of the gap in the clean case. Even for $\tau_Q = 0.5$, most of the error is constrained around the gap, indicating that the main contribution to the error in the DSF is a qualitative change in the overall broadness of the low-q, low-ω sector, even though the overall shape of the DSF does not change (as is seen in Fig. 4, *Left*).

In the case of unequal time correlators, shown in Fig. 4, *Center*, we see that the maximal (average in *Inset*) error in this case, for $\tau_Q = 100$, is also below 5% (1%), but we can see how the average error increases over time. While looking at the correlators directly could also be a way to study the ground-state fluctuation of the system (given that the effect of the imperfections is small), the interpretation of the data as a function of time can be much more challenging, especially for long times. This can be understood by considering the propagation of errors as a function of time, which takes place with a maximal velocity consistent with the Lieb–Robinson bounds. We show in *SI Appendix*, Fig. 5 the propagation of errors in the correlators as a function of time. With this in mind, we can note that the Fourier transform leading to the DSF allows one to account for all of the spatial and temporal data of the correlators, as well as understand and deal with errors arising from this imperfection model in a much simpler way.

Influence of Evolution Imperfections on DSF. In trapped-ions architectures, the spin–spin interactions are created by coupling the spin states to the normal modes of motion of the ions by laser

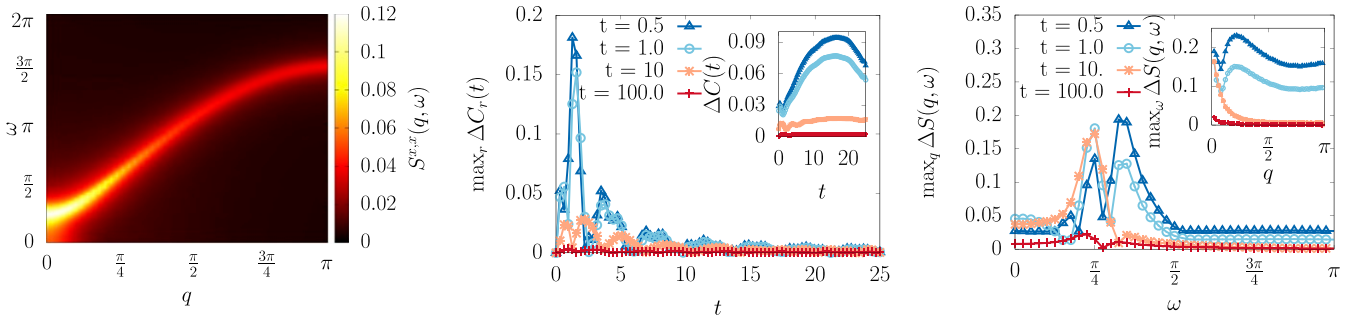

Fig. 4. Effect of finite preparation times τ_Q on the DSF of the short-range TFIM. We show numerical results for the DSF and unequal time-correlation functions of the short-range TFIM subject to different preparation time. (*Left*) DSF of the TFIM for a preparation time $\tau_Q = 0.5$. This can be directly compared to the imperfection free case shown in Fig. 2. (*Center*) Cuts of the absolute error for the unequal time-correlation function, depicted for a quantitative comparison. At short preparation times $\tau_Q = 0.5$ and $\tau_Q = 1$, we find significant deviations of local correlation functions. *Center*, *Inset* shows the averaged error in the correlators, which indicates that the deviation seen in the maximal error persists, and in fact increases, at all times on the level of uniform real-space average. (*Right*) Cuts in frequency and reciprocal space (*Inset*) of the DSF absolute error. We quantitatively verify the intuition given by *Left*. The DSF indeed encodes the correct physical information, despite the deviations in real space and the deformation of the low-ω sector. The low error intensity away from $\omega = \pi/4$ and $q = 0$ indicate that the gap remains open for $\tau_Q = 100$. Absence of errors for long preparation times at $q > 0$ and $\omega > \pi/4$ indicate that the two-particle continuum is not affected by these preparation times.

beams (65, 66) (*SI Appendix*, section I), obtaining a coupling strength directly proportional to the Rabi frequency of the ions. The lasers employed present intensity and phase oscillations which can be currently controlled up to a certain threshold (67). This induces a variation of the Rabi frequencies across the chain, resulting in interactions which are not uniform over time along the chain.

Globally Fluctuating Ising Coupling. We will study the particular case in which the intensity fluctuations of the lasers directly induce periodic fluctuations of the spin–spin interactions. We will model these evolution imperfections by modulating the Ising coupling as in Eq. **23**, with different amplitudes A and frequencies w.

In Fig. 5, we show the error analysis of the DSF and unequal time-correlation functions for the case of modulated Ising couplings. We have studied a range of frequencies from $w = 0.05$ to $w = 25$ and intensities in the range $A \in [0.01, 1]$. Here, where $J = 1$, a coupling intensity $A = 0.01$ correspond to a 1% fluctuation in the Ising coupling. Current experimental capabilities can constrain these parameters within the 1% threshold (68).

The effects are mainly noticed as a function of the coupling A. Concentrating on the error of the DSF shown in Fig. 5, *Left* and *Right*, we see that even the lowest coupling studied, $A = 1\% = 0.01$, can induce a maximal error of 15% in the DSF. The error is mostly concentrated around gap. Already for $A = 0.05$, we see that small broad peaks appear for $\omega > \pi/4$, while for $A = 0.5$, the shape of the DSF is changed, as indicated by the large errors all along the frequency axis in Fig. 5, *Left*. This can be understood by looking at Fig. 5, *Left*, comparing it with Fig. 2. Besides the overall decrease in intensity, the low-frequency shape of the two-particle continuum has changed, giving the maximum in Fig. 5, *Right* at $\omega = \pi/4$. There is also an increase of intensity at small q for a range of frequencies up to $\omega = \pi/2$.

In the case of the unequal time correlators, Fig. 5, *Center*, the error intensity is much higher, with a maximum of 65% at small times, which decays to close to zero, except for $A = 0.5$. This is an artifact generated by the error propagation in a Lieb–Robinson cone. Even if the maximal error is small, there is an overall error which increases with time, which indicates that long measurement times lead to the propagation of errors and to an, on average, very large inaccuracy in the correlators. As for the case of preparation imperfections, the error in the correlators can make for a hard determination of the propagation of excitations through the system. The DSF allows us to study these effects even in the presence of imperfections, given that the errors in this quantity are localized close to the maxima, and the overall shape of the two-particle continuum is minimally changed for small intensities of the fluctuating coupling.

It has to be pointed out that for slightly higher intensities of the fluctuating coupling, even for $A = 5\%$, small changes in the DSF are seen both in the frequency and reciprocal space axis. This indicates that this imperfection model has to be dealt with carefully in an experimental setup, as small increases in A can lead to appreciable effects in both the DSF and the unequal time correlators.

Lattice Imperfections. In a Rydberg atom setup, spin–spin interactions can be generated by applying a spin-dependent optical dipole force (18, 19) (*SI Appendix*, section I). Since the Rydberg atoms are not in the ground state once in the local trap, and the experiment is carried at a finite temperature, fluctuations in the atomic positions for each atom in each cycle of the experiment are introduced (18, 19), which will affect the Ising interaction (*SI Appendix*, Eq. **2**). In a typical experiment, the fluctuation of the position leads to a change in the Ising coupling between 0.1% and 0.2% (18, 19) from shot to shot. This can be empirically modeled as a random Ising interaction, as in Eq. **23**. On the other hand, the Rabi frequency is also not uniform along the chain. Since this frequency gives rise to the transverse field, this type of evolution imperfection can be studied as a random transverse field, as in Eq. **24**.

In a setup where ions are trapped by a linear Paul trap, spin–spin interactions can be obtained by applying off-resonant laser beams (65, 66). The Rabi frequency Ω_i can also vary across the chain from shot to shot (*SI Appendix*, Eq. **3**), inducing random Ising interactions.

For these cases, random transverse fields and Ising interactions, we show the results in *SI Appendix*, section II, since they are very similar to those found for the preparation imperfections. In both cases, we see that the majority of the imperfections are concentrated around the maximum of the DSF, where the gap is located. Strong random Ising interactions tend to close the gap, as can be seen in *SI Appendix*, section II, Figs. 1 and 3*C*. On the other hand, random transverse fields tend to open it (*SI Appendix*, Figs. 3 and 4*D*). In both these cases, for the experimentally tolerable imperfections of around 1%, the errors in the DSF and correlators are both reduced, leading to no noticeable effects in the DSF. While the errors in the correlators (*SI Appendix*, section II, Figs. 1 and 2) are also small, the average error increases

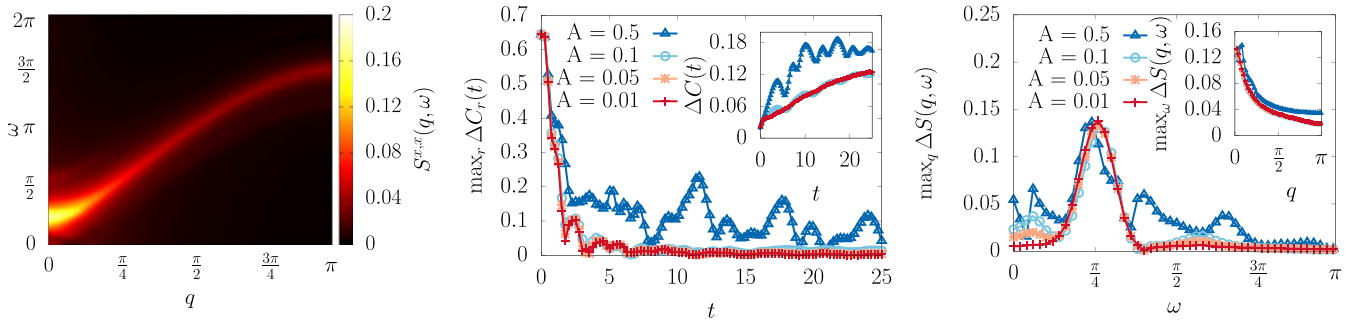

Fig. 5. Effect of globally fluctuating Ising couplings on the DSF of the short-range TFIM. We show numerical results for the DSF of the short-range TFIM subject to the imperfection model Eq. **23** with Ising couplings harmonically modulated for amplitudes. (*Left*) DSF of the TFIM for an Ising coupling modulated by $A = 10\%$. This can be directly compared to the imperfection-free case shown in Fig. 2. (*Center*) Cuts of the absolute error for the unequal time-correlation function, shown for quantitative comparison. We see that at short times, there are significant deviations of the local unequal time-correlation functions. *Center*, *Inset* shows that this deviation increases, at all times on the level of uniform real-space average. (*Right*) Cuts in frequency and reciprocal space (*Inset*) of the DSF absolute error. We quantitatively verify the intuition given by *Left*. The DSF indeed encodes the correct physical information, despite the deviations in real space and the deformation of the low-ω sector. The gap remains open for the lowest imperfection level. The broadness of the maxima in the frequency cuts indicate that the gap is shifted with respect to the exact solution. *Right, Inset* shows that the effect over momentum space does not decay to zero, coming from the lower intensity in the DSF signal in comparison to the clean solution, and not from a deformation of the two-particle continuum.

with time. In this sense, long measurement times can lead to very large errors, rendering the results analyzed purely via correlation functions highly unreliable.

We note that the regime in which randomness is large is interesting in itself, as it offers the chance to directly probe the effect of random disorder in spin chains via time-dependent observables, and the DSF in particular, in near-term quantum devices.

Influence of Experimental Imperfections on the DSF of the Long-Range TFIM

In the previous section, we assessed the accuracy of a DSF measurement for the short-range TFIM using quantum simulators and showed that the DSF is well behaved in the presence of experimental imperfections, even at large system sizes. Now, we will put forward the idea that quantum simulators can recover the DSF of long-range models in such a way that the deviations induced by the error sources do not obscure the overall features of the DSF and that this can be done for system sizes larger than what state-of-the-art classical simulations can treat. To show this, we will numerically study the long-range TFIM in the presence of the same experimental imperfections as for the short-range TFIM.

In Fig. 3, we show the DSF in the absence of imperfections for three different values of α. In *SI Appendix*, section IV, we show the results for $\alpha = 2$, 3, and 6. Furthermore, in *SI Appendix*, section V, we show the heat maps for the unequal time correlations with respect to the middle of the chain, $C^{x,x}_{i,5}(t)$. In the regime $1 < \alpha < 2$, our results exhibit a particular signature in the DSF which has no $\omega-$dependence. For higher values of α, remnants of this behavior are noticed, but an $\omega-$dependence is recovered. For $\alpha > 3$, we recover the cosine-shaped two-particle continuum. These results, especially the absence of ω-dependence for $\alpha < 2$, indicate that the signatures of excitation confinement, which have been recently proposed (26, 42, 58), can be observed in dynamical quantum simulators via the DSF by employing our proposed method.

In *SI Appendix*, section IV, we show a typical case for the maximal error as a function of frequency (reciprocal space) Eq. **26** (Eq. **27**) in the case of random transverse fields. There, we can see that the overall behavior of the error is very similar to that for the short-range TFIM. There is a large error around the gap, with small fluctuations at other values of ω for strong imperfections. For small imperfection levels (1 to 5%), the error in the DSF is negligible, for all imperfection models, as it was found for the short-range TFIM.

In Fig. 6, we show the integrated error (30) as a function of the interaction range α for the models corresponding to evolution imperfections. Fig. 6*A* shows the error for the case of laser-intensity fluctuations, while Fig. 6 *B* and *C* show the random fields and random interactions, respectively. In both cases, we see two regimes, where the error drastically changes for $1 < \alpha < 3$, while it stabilizes for $\alpha > 3$. For the laser-intensity fluctuations, the error monotonically increases in the first regime and saturates in the second. On the other hand, the opposite behavior is observed for the lattice imperfections, where the error decreases as a function of α.

While the errors change as the value of α is modified, at the imperfection levels present in the current architectures, the integrated error is negligible, indicating that the DSF at all values of α can be probed by using these setups, and the measurement would yield accurate results.

System-Size Scaling for Long-Range Models. Now, we concentrate on the scaling properties of the DSF of the long-range TFIM. We study system sizes ranging from $L = 9$ to $L = 14$ sites employing full exact diagonalization and analyze how the integrated error changes with size. Since current architectures can simulate up to approximately 50 sites (18, 19), this is a playground in which the DSF can be employed to explore the potential of dynamical analog quantum simulators. We show the scaling properties of the error for $\alpha = 1.5$ and $\alpha = 6$. In Fig. 7, we show the integrated error originating from the evolution imperfections, as a function of system size, for the two aforementioned values of α.

For imperfection levels below 10%, the integrated error is relatively constant over the full range of system sizes studied here. When the imperfection level is reduced further, below 5% (within current experimental capabilities), it becomes negligible for all system sizes and interaction ranges. Our data suggest that the error remains constant and small at even the smallest sizes studied here, indicating that the integrated DSF error is intensive with respect to the system sizes, and, as such, we expect that the scaling properties will be maintained for larger chains. Furthermore, our data indicate that a dynamical quantum simulator can measure the DSF of the long-range TFIM accurately, even in the presence of realistic experimental imperfections, for system sizes considerably bigger than what is currently achievable with

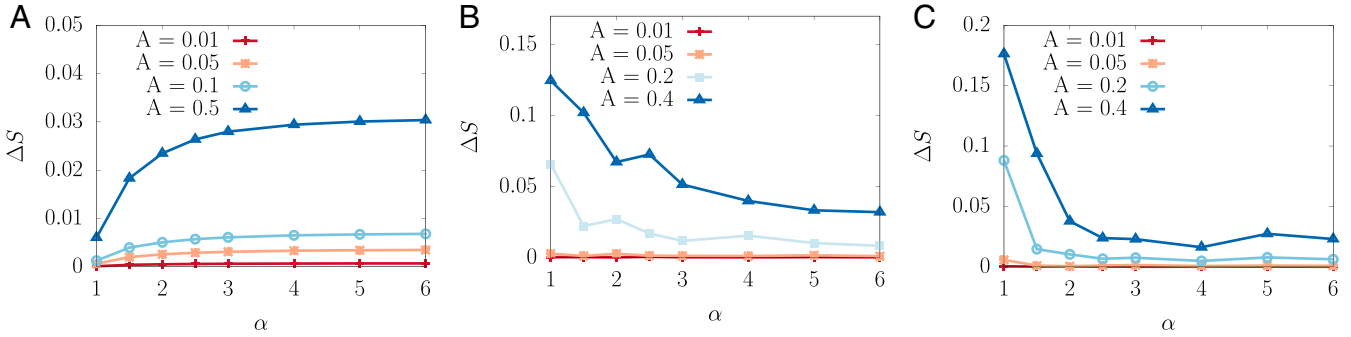

Fig. 6. Effect of experimental imperfections in the DSF for the long-range TFIM. Average error, ΔS, as a function of the interaction range, α, for $L = 14$ sites is shown. (*A*) Effects of Ising couplings harmonically modulated (Eq. **23**). The error is minimal at $\alpha = 1$, within the confined phase, and saturating at $\alpha > 3$, when the system approaches the short-range TFIM. (*B* and *C*) Effect of lattice imperfection for random fields (*B*) and random interactions (*C*). For both these cases, the effect is the same: The DSF is highly susceptible to randomness at low values of α, and it monotonically becomes more robust as α is increased, recovering the short-range behavior for $\alpha \to \infty$. A physical interpretation of the effect on the excitations of these imperfection models on the DSF is beyond the scope of this work, as the presence of excitation confinement in the long-range model has been proposed recently (26, 42, 58). At the experimental levels of control currently available, the integrated error is minimal, and the overall shape of the DSF is unchanged, indicating that quantum simulators can probe the regime of interactions studied in this work, $1 < \alpha < 6$, and obtain accurate DSFs for system sizes bigger than what state-of-the-art classical algorithms can achieve.

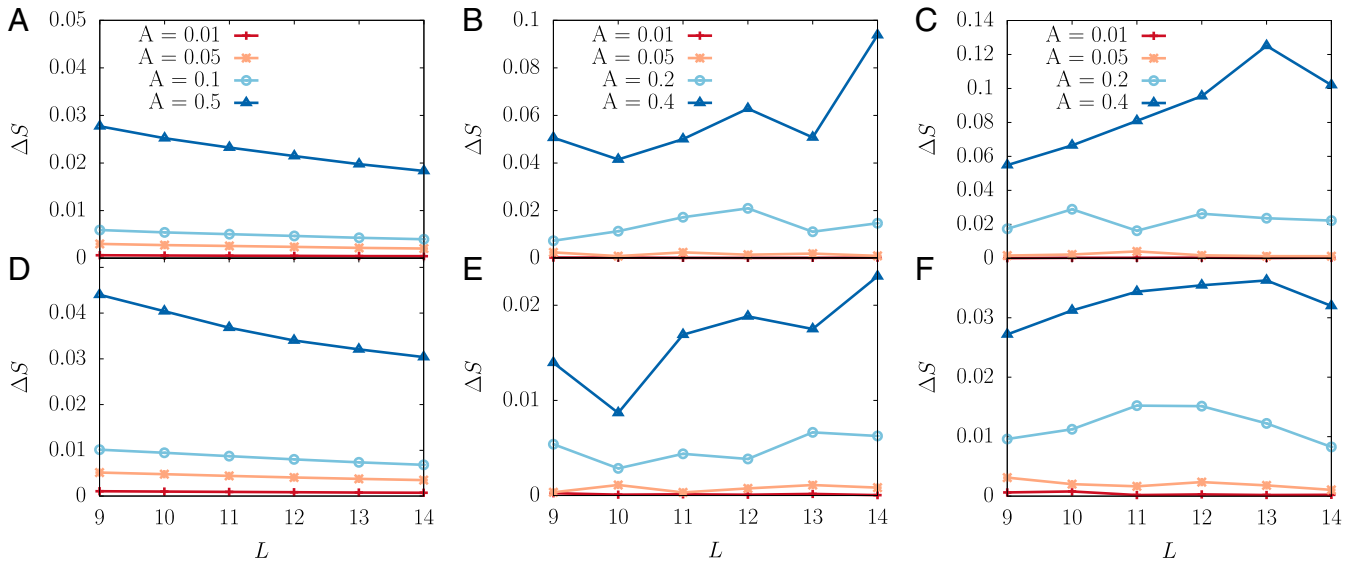

Fig. 7. Average DSF error as a function of system size for the long-range TFIM. Average error in the DSF, ΔS, arising from the different imperfection models, is shown. We show the numerical results for two interaction ranges. In *A*–*C* , we show the results for the interaction exponent $\alpha = 1.5$, while in *D*–*F*, we show the results for $\alpha = 6$. (*A* and *D*) We show the effects of harmonically modulated Ising interactions. (*B* and *E*) Average error in the DSF for the case of random interactions. (*C* and *F*) Average error in the DSF arising from random transverse fields. For all these cases, at the experimental level of control over the different imperfections, $A < 5\%$, the error is small and constant along the whole range of sizes. When the imperfection level is below 20%, it becomes negligible for all system sizes and interaction ranges. At the current levels of experimental control, the error remains constant and small, even at the smallest size studied here, with the DSF remaining unchanged through the entire α range employed in this work.

numerical simulations, thus paving the way toward a practical quantum advantage.

Conclusions

In this work, we propose the observation of DSFs as a practical application of dynamical quantum simulators. We have shown that the BQP-hardness of general local Hamiltonian time evolution is inherited by the DSF, suggesting that its efficient classical computation might be infeasible also for practically relevant instances. In this endeavor, we build on the measurement protocol of ref. 33 and tomographic ideas, allowing us to measure the DSF in several different quantum architectures. These architectures include those of trapped ions, Rydberg atoms, cold atoms in optical lattices, and superconducting qubits.

To emphasize the feasibility of this approach, we study the robustness of the DSF against several meaningful models of experimental imperfections for the short- and long-range TFIMs. Our results for the short-range TFIM indicate that the overall features of the DSF are preserved when one considers state-of-the-art setups, their associated experimental imperfections, and the current level of control over them. For the long-range model, we observe that the effects of imperfections at the current experimental levels and for the system sizes studied in this work do not change the DSF. We have brought our findings into contact with signatures of the exotic physics in the long-range TFIM, in particular, the confinement of excitations which has been recently reported. Unlike previous studies, we observe the signatures of confinement in both the DSF and correlators in equilibrium, i.e., without the need to quench the Hamiltonian, with equilibrium being a fundamental requirement of our proposed DSF measurement protocol. Following the study of these imperfections, we carry out a system size scaling, which indicates that the errors of the DSF induced by these imperfections are controlled over the whole range of sizes—remaining small and constant. This indicates that for the imperfections considered in this work, a quantum-simulation experiment with system sizes considerably bigger than what state-of-the-art classical algorithms can achieve is expected to yield accurate results. It is worth pointing out that the evolution times that can be achieved experimentally will depend on the coherence time of the experiment, which directly depends on the system sizes implemented. For example, in the case of Rydberg atoms, it has been reported that the coherence time scales approximately inversely with the number of atoms (69, 70), while for trapped ions, the ratio of spontaneous emission for the long-range TFIM grows as the square root of the number of atoms (19). However, even for system sizes of 100 atoms, the coherence times would be sufficient to probe the DSF and the excitation confinement in the long-range TFIM.

We therefore argue that the measurement of DSFs in quantum simulators provides a useful tool to assess time-dependent quantities of key importance in condensed-matter physics and further place quantum simulators into the realm of quantum technological devices (71). We hope that the present work stimulates further assessments of this quantity in other physical contexts.

Materials and Methods

Method. We employed exact diagonalization to study the long-range TFIM for system sizes up to $L = 14$ sites, while we employed free fermionic technique, as described in *SI Appendix*, to study the short-range case for systems up to $L = 50$ sites. In both cases, the time evolution was done in an open boundary chain, for a time $t \in [0, L/2]$.

Data Availability. All study data are included in the article and supporting information.

ACKNOWLEDGMENTS. M.L.B. thanks Dante Kennes, Markus Heyl, David Luitz, Pedram Roushan, Pietro Silvi, Jan Carl Budich, Bela Bauer, and Thierry Giamarchi for fruitful discussions. J.E. thanks Holger Boche for discussions. This work was supported by the European Research Council (Taming Non-Equilibrium Quantum Systems); the Templeton Foundation; the Foundational Questions Institute; Deutsche Forschungsgemeinschaft Grants EI 519/14-1, EI 519/15-1, CRC 183, and FOR 2724; and MATH+. This work was also supported by European Union Horizon 2020 research and innovation program under Grant 817482 (Programmable Atomic Large-Scale Quantum Simulation). J.B.-V. was supported by the European Union's Horizon 2020 research and innovation program under the Marie Skłodowska-Curie Grant 754446 and University of Granada Research and Knowledge Transfer Fund–Athenea3i.

1. W. M. C. Foulkes, L. Mitas, R. J. Needs, G. Rajagopal, Quantum Monte Carlo simulations of solids. *Rev. Mod. Phys.* **73**, 33–83 (2001).
2. R. M. Noack, S. R. Manmana, Diagonalization and numerical renormalization group based methods for interacting quantum systems. *AIP Conf. Proc.* **789**, 93–163 (2005).
3. R. Orus, Tensor networks for complex quantum systems. arXiv:1812.04011 (10 December 2018).
4. E. J. Chaisson, E. Chaisson, *Cosmic Evolution* (Harvard University Press, Cambridge, MA, 2001).
5. D. L. Cosmogenesis, *The Growth of Order in the Universe* (Oxford University Press, Oxford, UK, 1991).
6. S. Aaronson, NP-complete problems and physical reality. arXiv:quant-ph/0502072 (12 February 2005).
7. S. Aaronson, BQP and the polynomial hierarchy arXiv:0910.4698 (25 October 2009).
8. R. Ran, A. Tal, "Oracle separation of BQP and PH" in *Proceedings of the 51st Annual ACM SIGACT Symposium on Theory of Computing* (Association for Computing Machinery, New York, 2019), pp. 13–23.
9. M. Marvian, D. A. Lidar, I. Hen, On the computational complexity of curing the sign problem. *Nat. Commun.* **10**, 1571 (2019).
10. J. Klassen *et al.*, Hardness and ease of curing the sign problem for two-local qubit Hamiltonians. arXiv:1906.08800 (20 June 2019).
11. D. Hangleiter, I. Roth, D. Nagaj, J. Eisert, Easing the Monte Carlo sign problem. arXiv:1906.02309 (5 June 2019).
12. J. I. Cirac, P. Zoller, Goals and opportunities in quantum simulation. *Nat. Phys.* **8**, 264–266 (2012).
13. J. Eisert, M. Friesdorf, C. Gogolin, Quantum many-body systems out of equilibrium. *Nat. Phys.* **11**, 124–130 (2015).
14. T. Fukuhara *et al.*, Microscopic observation of magnon bound states and their dynamics. *Nature* **502**, 76–79 (2013).
15. T. Fukuhara *et al.*, Quantum dynamics of a mobile spin impurity. *Nat. Phys.* **9**, 235–241 (2013).
16. M. Cheneau *et al.*, Light-cone-like spreading of correlations in a quantum many-body system. *Nature* **481**, 484–487 (2012).
17. J. Simon *et al.*, Quantum simulation of antiferromagnetic spin chains in an optical lattice. *Nature* **472**, 307–312 (2011).
18. H. Bernien *et al.*, Probing many-body dynamics on a 51-atom quantum simulator. *Nature*, **551**, 579–584 (2017).
19. J. Zhang *et al.*, Observation of a many-body dynamical phase transition with a 53-qubit quantum simulator. *Nature* **551**, 601–604 (2017).
20. J. G. Bohnet *et al.*, Quantum spin dynamics and entanglement generation with hundreds of trapped ions. *Science* **352**, 1297–1301 (2016).
21. R. Islam *et al.*, Onset of a quantum phase transition with a trapped ion quantum simulator. *Nat. Commun.* **2**, 377 (2011).
22. S. Trotzky *et al.*, Probing the relaxation toward equilibrium in an isolated strongly correlated one-dimensional Bose gas. *Nat. Phys.* **8**, 325–330 (2012).
23. R. Coldea *et al.*, Quantum criticality in an Ising chain: Experimental evidence for emergent E_8 symmetry. *Science* **327**, 177–180 (2010).
24. C. J. Jia *et al.*, Persistent spin excitations in doped antiferromagnets revealed by resonant inelastic light scattering. *Nat. Commun.* **5**, 3314 (2014).
25. R. Landig, F. Brennecke, R. Mottl, T. Donner, T. Esslinger, Measuring the dynamic structure factor of a quantum gas undergoing a structural phase transition. *Nat. Commun.* **6**, 7046 (2015).
26. F. Liu *et al.*, Confined quasiparticle dynamics in long-range interacting quantum spin chains. *Phys. Rev. Lett.* **122**, 150601 (2019).
27. D. J. Luitz, Y. Bar Lev, Emergent locality in systems with power-law interactions. *Phys. Rev. A* **99**, 010105(R) (2019).
28. K. R. Fratus, M. Srednicki, Eigenstate thermalization and spontaneous symmetry breaking in the one-dimensional transverse-field Ising model with power-law interactions arXiv:1611.03992 (12 November 2016).
29. P. Hauke, L. Tagliacozzo, Spread of correlations in long-range interacting quantum systems. *Phys. Rev. Lett.* **111**, 207202 (2013).
30. S. Sachdev, *Quantum Phase Transitions* (Cambridge University Press, Cambridge, UK, ed. 2, 2011).
31. P. Roushan *et al.*, Spectroscopic signatures of localization with interacting photons in superconducting qubits. *Science* **358**, 1175–1179 (2017).
32. D. Barredo *et al.*, Coherent excitation transfer in a spin chain of three Rydberg atoms. *Phys. Rev. Lett.* **114**, 113002 (2015).
33. M. Knap *et al.*, Probing real-space and time-resolved correlation functions with many-body Ramsey interferometry. *Phys. Rev. Lett.*, **111**, 147205 (2013).
34. B. T. Yoshimura, J. K. Freericks, Measuring nonequilibrium retarded spin-spin Green's functions in an ion-trap-based quantum simulator. *Phys. Rev. A* **93**, 052314 (2016).
35. G. Pagano *et al.*, Quantum approximate optimization with a trapped-ion quantum simulator. arXiv:1906.02700 (6 June 2019).
36. M. Baiesi, C. Maes, B. Wynants, Fluctuations and response of nonequilibrium states. *Phys. Rev. Lett.* **103**, 010602 (2009).
37. E. A. Calzetta, B.-L. B. Hu, *Nonequilibrium Quantum Field Theory* (Cambridge Monographs on Mathematical Physics, Cambridge University Press, Cambridge, UK, 2008).
38. J. Kempe, A. Kitaev, O. Regev, The complexity of the local Hamiltonian problem. *SIAM J. Comput.* **35**, 1070–1097 (2004).
39. D. Gosset, B. M. Terhal, A. Vershynina, Universal adiabatic quantum computation via the space-time circuit-to-Hamiltonian construction. *Phys. Rev. Lett.* **114**, 140501 (2015).
40. S. Lloyd, B. M. Terhal, Adiabatic and Hamiltonian computing on a 2D lattice with simple 2-qubit interactions. *New J. Phys.* **18**, 023042 (2016).
41. A. Ciani, B. Terhal, D. DiVinzenzo, Hamiltonian quantum computing with superconducting qubits. *Quant. Sc. Tech.* **4**, 035002 (2019).
42. A. Lerose, B. Žunkovič, A. Silva, A. Gambassi, Quasilocalized excitations induced by long-range interactions in translationally invariant quantum spin chains. *Phys. Rev. B* **99**, 121112(R) (2019).
43. O. Derzhko, T. Krokhmalskii, Dynamic structure factor of the spin-$\frac{1}{2}$ transverse Ising chain. *Phys. Rev. B* **56**, 11659–11665 (1997).
44. G. M. Crosswhite, A. C. Doherty, G. Vidal, Applying matrix product operators to model systems with long-range interactions. *Phys. Rev. B* **78**, 035116 (2008).
45. D. Jaschke, K. Maeda, J. D. Whalen, M. L. Wall, L. D. Carr, Critical phenomena and Kibble–Zurek scaling in the long-range quantum Ising chain. *New J. Phys.* **19**, 033032 (2017).
46. S. N. Saadatmand, S. D. Bartlett, I. P. McCulloch, Phase diagram of the quantum Ising model with long-range interactions on an infinite-cylinder triangular lattice. *Phys. Rev. B* **97**, 155116 (2018).
47. J. Haegeman *et al.*, Time-dependent variational principle for quantum lattices. *Phys. Rev. Lett.* **107**, 070601 (2011).
48. M. P. Zaletel, R. S. K. Mong, C. Karrasch, J. E. Moore, F. Pollmann, Time-evolving a matrix product state with long-ranged interactions. *Phys. Rev. B* **91**, 165112 (2015).
49. T. Hashizume, I. P. McCulloch, J. C. Halimeh, Dynamical phase transitions in the two-dimensional transverse-field Ising model. arXiv:1811.09275 (22 November 2018).
50. Z. Zhu, G. Sun, W.-L. You, D.-N. Shi, Fidelity and criticality of a quantum Ising chain with long-range interactions. *Phys. Rev. A* **98**, 023607 (2018).
51. D. Amit, J. K. Bhattacharjee, Phase transitions in the quantum Ising and rotor models with a long-range interaction. *Phys. Rev. B* **64**, 184106 (2001).
52. T. Blanchard, M. Picco, M. A. Rajabpour, Influence of long-range interactions on the critical behavior of the Ising model. *EPL* **101**, 56003 (2013).
53. G. Piccitto, B. Žunkovič, A. Silva, Dynamical phase diagram of a quantum Ising chain with long-range interactions. *Phys. Rev. B* **100**, 180402 (2019).
54. M. Kastner, Diverging equilibration times in long-range quantum spin models. *Phys. Rev. Lett.* **106**, 130601 (2011).
55. I. Homrighausen, N. O. Abeling, V. Zauner-Stauber, J. C. Halimeh, Anomalous dynamical phase in quantum spin chains with long-range interactions. *Phys. Rev. B* **96**, 104436 (2017).
56. A. S. Buyskikh, M. Fagotti, J. Schachenmayer, F. Essler, A. J. Daley, Entanglement growth and correlation spreading with variable-range interactions in spin and fermionic tunneling models. *Phys. Rev. A* **93**, 053620 (2016).
57. M. B. Hastings, T. Koma, Spectral gap and exponential decay of correlations. *Commun. Math. Phys.* **265**, 781–804 (2006).
58. R. Verdel, F. Liu, S. Whitsitt, A. V. Gorshkov, M. Heyl, Real-time dynamics of string breaking in quantum spin chains. arXiv:1911.11382 (26 November 2019).
59. J. Eisert *et al*, Quantum certification and benchmarking. *Nat. Rev. Phys.* **2**, 382–390 (2020).
60. J. Dziarmaga, Dynamics of a quantum phase transition: Exact solution of the quantum Ising model. *Phys. Rev. Lett.* **95**, 245701 (2005).
61. W. H. Zurek, U. Dorner, P. Zoller, Dynamics of a quantum phase transition. *Phys. Rev. Lett.* **95**, 105701 (2005).
62. L. Cincio, J. Dziarmaga, M. M. Rams, W. H. Zurek, Entropy of entanglement and correlations induced by a quench: Dynamics of a quantum phase transition in the quantum Ising model. *Phys. Rev. A* **75**, 052321 (2007).
63. L. Cincio, J. Dziarmaga, J. Meisner, M. M. Rams, Dynamics of a quantum phase transition with decoherence: Quantum Ising chain in a static spin environment. *Phys. Rev. B* **79**, 094421 (2009).
64. D. M. Kennes, C. Karrasch, A. J. Millis, Loschmidt-amplitude wave function spectroscopy and the physics of dynamically driven phase transitions. arXiv:1809.00733 (3 September 2018).
65. K. Kim *et al*, Quantum simulation of frustrated Ising spins with trapped ions. *Nature* **465**, 590–593 (2010).
66. E. E. Edwards *et al*, Quantum simulation and phase diagram of the transverse-field Ising model with three atomic spins. *Phys. Rev. B* **82**, 060412(R) (2010).
67. S. Schneider, G. J. Milburn, Decoherence in ion traps due to laser intensity and phase fluctuations. *Phys. Rev. A* **57**, 3748–3752 (1998).
68. A. Friedenauer, H. Schmitz, J. T. Glueckert, D. Porras, T. Schaetz, Simulating a quantum magnet with trapped ions. *Nat. Phys.* **4**, 757–761 (2008).
69. M. Ebert, M. Kwon, T. G. Walker, M. Saffman, Coherence and Rydberg blockade of atomic ensemble qubits. *Phys. Rev. Lett.* **115**, 093601 (2015).
70. H. Levine *et al*, High-fidelity control and entanglement of Rydberg-atom qubits. *Phys. Rev. Lett.* **121**, 123603 (2018).
71. A. Acin *et al*, The European quantum technologies roadmap. *New J. Phys.* **20**, 080201 (2018).